Journal of Nuclear Materials 395 (2009) 37–44

Contents lists available at ScienceDirect

Journal of Nuclear Materials

journal homepage: www.elsevier.com/locate/jnucmat

Post-irradiated microstructural characterisation of cold-worked SS316L by X-ray diffraction technique

P. Mukherjee [a,*], A. Sarkar [b], M. Bhattacharya [a], N. Gayathri [a], P. Barat [a]

[a] Variable Energy Cyclotron Centre, 1/AF Bidhan Nagar, Kolkata 700064, India
[b] Mechanical Metallurgy Section, Bhabha Atomic Research Centre, Mumbai 400 085, India

ARTICLE INFO

Article history:
Received 22 June 2009
Accepted 27 September 2009

ABSTRACT

In this paper, an attempt has been made to understand the mechanisms of the evolution of defects in SS316L (20% cold-worked) when irradiated with 145 MeV Ne^{6+} at a dose range of 10^{17} to 10^{19} Ne^{6+}/m^2. The microstructural parameters of Ne-irradiated samples have been characterised by X-ray Diffraction Line Profile Analysis using different model-based approaches like modified Williamson–Hall Technique, Modified Rietveld Analysis and Pattern Decomposition using MarqX. The domain size, microstrain and density of dislocation of the irradiated alloy have been estimated as a function of dose. Radiation induced recovery of the prior existed dislocation network has been manifested by the decrease in the microstrain values with increasing dose of irradiation. Domain size and microstrain values decreased initially with dose and finally attained a saturation.

1. Introduction

Materials degradation due to radiation damage in nuclear reactor core components has been investigated for more than four decades [1–3]. It is a continuing effort to understand how the degradation occurs under irradiation in order to provide guidance in the development of new and more resistant alloys and to optimize the performance of the existing alloys. Consequently, the materials development community continues to rely on developing a fundamental understanding of the various processes that are involved in radiation effects of materials, particularly primary damage production, microstructural evolution, and the changes in mechanical, physical and chemical properties [4–6]. This understanding definitely helped to provide a superior methodology for interpreting and applying available data to the prediction of the property and the other microstructural changes for the structural materials of the reactor of interest.

Austenitic stainless steel 316L are widely used as a structural material in fast reactors and light water cooled power reactors and also is a tentative candidate material for the fusion reactor and accelerator-driven systems [7–9]. Pronounced changes in the microstructural behavior occur in austenitic stainless steels as a function of irradiation temperature. The microstructural response can be roughly divided into two major temperature regimes. In the low-temperature regime (<573 K), the microstructure of austenitic stainless steels is dominated primarily by small defect clusters, faulted dislocation loops, and network of dislocations if the latter existed prior to irradiation [10]. The densities of defect clusters and faulted loops are relatively independent of irradiation temperature in this low-temperature regime. At high temperature regime (~573 to 973 K), the microstructure evolution is complex and consists of helium bubbles, voids, dislocation loops and network of dislocations, and various types of precipitates [11,12].

In spite of several irradiation studies performed on austenitic stainless steel over the past 25 years, still there is lack of low fluence data for this alloy. In the review of Zinkle et al. [13] on the dose dependence microstructural evolution in neutron-irradiated austenitic stainless steel, the author clearly mentioned that there is a need for further irradiation experiments on the alloy as systematic data at low temperature and low doses are not available. Allen et al. [14] have studied void size distribution, swelling rate and grain boundary segregation over a dose rate of 1–56 dpa on 20% cold-worked SS316. Recently, microstructure evolution in low nickel austenitic stainless steel at a dose rate of 1.7–20 dpa has been studied [15].

Keeping in view of the importance of these studies, an attempt has been made to understand the evolution of defects in SS316L (20% cold-worked) at low dose and at room temperature, which has been described as a transient regime before attaining the steady state of the microstructural components [13].

We have carried out irradiation with 145 MeV Ne^{6+} on 20% cold-worked SS316L at low doses in the dose range of 10^{17} to 10^{19} Ne^{6+}/m^2. Several techniques of X-ray Diffraction Line Profile Analysis (XRDLPA) have been used to evaluate the effect of the irradiation on the microstructure of the material. Since, ion-irradiation

* Corresponding author. Tel.: +91 33 23371230; fax: +91 33 23346871.
E-mail address: paramita@veccal.ernet.in (P. Mukherjee).

0022-3115/$ - see front matter © 2009 Elsevier B.V. All rights reserved.
doi:10.1016/j.jnucmat.2009.09.013

produces inhomogeneous damage profile, the irradiated microstructure will also be spatially heterogeneous. Hence, the study of statistically averaged microstructural parameters and their variations with increasing dose of irradiation are of utmost importance to understand the mechanism of radiation damage. XRDLPA evaluates the microstructural parameters in a statistical manner averaged over a volume of 10^9 μm^3. Hence, the bulk damage can be assessed by this analysis. Different techniques of XRDLPA have been widely applied successfully for the evaluation of microstructural parameters in deformed metals and alloy systems [16–19]. In our earlier studies, we had also characterised the microstructural variation due to irradiation with the proton and the oxygen ions on zirconium and titanium based alloys by XRDLPA [20–23].

In this work, three different model-based approaches: (1) Williamson–Hall Technique, (2) a Modified Rietveld Analysis, and (3) Pattern Decomposition using MarqX of XRDLPA have been used. The domain size, microstrain and the density of dislocation of the irradiated alloy have been estimated as a function of dose.

2. Experimental

Nuclear grade SS316L (20% cold-worked) samples having dimension of 20 × 20 × 1 mm (t) were mounted on an aluminium flange and then irradiated with 145 MeV Ne^{6+}ions from Variable Energy Cyclotron (VEC), Kolkata, India. The irradiation doses were 1×10^{17}, 5×10^{17}, 1×10^{18}, 3×10^{18}, 7×10^{18}, 1.2×10^{19}, and 2.5×10^{19} Ne^{6+}/m^2. The ion current used in the experiment was 150 nA. The flange used for the irradiation was cooled by a continuous flow of water. During irradiation, the temperature of the sample did not rise above 313 K as measured by the thermocouple connected very close to the sample. The range of the ions in these materials and the displacement per atoms (dpa) were obtained by Monte-Carlo simulation technique using the code SRIM 2000 [24].

X-ray Diffraction (XRD) profile for each irradiated sample has been recorded by Bruker D8 Advance X-ray diffractometer using MoK_α radiation. The range of 2θ was from 18° to 41° and a step scan of 0.02° was used. The time per step was 60 s.

3. Method of analysis

There are two categories of structural imperfections which give rise to a spread of intensity around each reciprocal-lattice points and thus modify the diffraction line profiles by a measurable amount. The first is the finite size of the domains, over which the diffraction is coherent, measured in the direction of the diffraction vector for a given reflection. This can be the mean thickness of the individual crystallites, it can also relate to a sub-domain structure, i.e. the separation of the regions bounded by the low angle grain boundaries and also the structural mistakes [25]. During heavy ion irradiation, the damage associated with Ne^{6+} beam was quite extensive and a highly localized concentration of defects, particularly vacancies and interstitials, are produced. These vacancies agglomerate and collapse to form dislocation loops. These loops interact with the pre-existing dislocations and forms incoherent regions with respect to each other. Each region has been termed as domain in the following discussion. The second category of the structural imperfections is based on the distortion of the crystal lattice, which amounts to a variation of the interplanar spacing within the domains. This can arise from the microstrain, due to an applied or residual stress, or from a compositional gradient in the sample. Dislocations contribute to both categories of broadening of the X-ray diffraction line profile. There will be a size contribution due to their mean separation, inversely proportional to the dislocation density, and microstrain arising from internal stress fields [25]. There are several model-based approaches which help to separate these two independent effects by fitting the diffraction peaks with suitable mathematical functions. In the present paper, different model-based approaches as mentioned earlier, have been adopted to assess the dose-dependent variation of domain size and microstrain in 20% cold-worked SS316L samples.

3.1. Williamson–Hall Technique

3.1.1. The modified Williamson–Hall plot

Taking into account that size and strain broadening are diffraction order independent and order dependent respectively, Williamson and Hall [26] suggested that the Full Width at Half-Maximum (FWHM) of the line profiles can be written as the sum of the two broadening effects [27]:

$$\Delta K = 0.9/D + \Delta K_D \tag{1}$$

Here, $K = 2\sin\theta/\lambda$, $\Delta K = 2\cos\theta(\Delta\theta)/\lambda$, ΔK_D is the strain contribution to line broadening and D is the volume averaged domain size. θ, $\Delta\theta$ and λ are the diffraction angle, FWHM and the wavelength of X-rays, respectively. In dislocated crystal, this relation does not hold good. Recently, Ungár and co-workers [27–29] have proposed a modified version the W–H plot assuming that strain broadening is caused only by dislocations. The modified WH relation is:

$$\Delta K \cong 0.9/D + \xi(K\bar{C}^{1/2}) + \gamma(K^2\bar{C}) \tag{2}$$

where ξ and γ are constants depending on the effective outer cut-off radius of the dislocation and the Burgers vector. However, ξ depends on the density of dislocations, while γ is related to the fluctuations in the density of dislocations [27–29]. Here, $\bar{C}$ is the average contrast factor of the dislocations depending on the relative positions of the diffraction vector.

Broadening of the diffraction peaks are also affected by the presence of planar defects. According to Warren [30], if stacking fault, twin boundaries or both are present in the crystal, the apparent domain size becomes smaller than the true particle size. Ungár et al. [29] incorporated the effect of twinning and faulting into the modified W–H plot. With this modification the Eq. (2) has been written as

$$\Delta K - \varsigma W(K) \cong 0.9/D + \xi(K\bar{C}^{1/2}) + \gamma(K^2\bar{C}) \tag{3}$$

where ς is related to the density of deformation faults (α) and twin boundaries (Γ) and $W(K)$ is connected to various crystallographic parameters. The detailed relations can be found in Ref. [30]. Warren determined the values of $W(K)$ for different peaks which can be obtained from Refs. [29,30].

3.2. Modified Rietveld Technique

In this method, the diffraction profile has been modeled by a pseudo-Voigt (pV) function using the program LS1 [31].

This program includes the simultaneous refinement of the crystal structure and the microstructural parameters like the domain size and the microstrain within the domain. The method involves the Fourier analysis of the broadened peaks. Considering an isotropic model, the lattice parameters (a), surface weighted average domain size (D_s) and the average microstrain $\langle\varepsilon_L^2\rangle^{\frac{1}{2}}$ were used simultaneously as the fitting parameters to obtain the best fit. The effective domain size (D_e) with respect to each of the fault-affected crystallographic plane was then refined to obtain the best fitting parameter.

The dislocation density ρ_e at each crystallographic plane has been estimated from the relation [32] $\rho = (\rho_D\rho_S)^{\frac{1}{2}}$, where, $\rho_D = \frac{3}{D_e^2}$ (dislocation density due to domain on a particular crystallographic plane) and $\rho_S = k\langle\varepsilon_L^2\rangle/b^2$ (dislocation density due to strain), k is the

material constant and b is the modulus of the Burger's vector, $\frac{1}{2}[1\,1\,0]$.

3.3. Pattern Decomposition using MarqX

This is a whole powder pattern fitting technique [33] based on the unconstrained profile fitting (Pattern Decomposition). Pseudo-Voigt (pV) function has been used to fit the diffraction profile. Profile modeling consists of the refinement of the peak position (2θ), maximum intensity, Half Width at Half-Maximum ($HWHM$) and pV mixing factor (η).

The integral breadth (β) of a pV function can be written as [33]:

$$\beta_{pV} = HWHM[(1-\eta)(\pi/\ln 2)^{1/2} + \eta\pi] \quad (4)$$

The knowledge of $HWHM$, η, β permits the calculation of Voigt parameter $\phi = \frac{2HWHM}{\beta}$ [34]. The corresponding Lorentz and Gauss components of the integral breadth (β_{gL}, β_{fL}, β_{gG}, and β_{fG}, respectively) can be calculated from [35]

$$\beta_{hL} = \beta_{gL} + \beta_{fL} \quad (5)$$

$$\beta_{hG} = (\beta_{gG}^2 + \beta_{fG}^2)^{1/2} \quad (6)$$

where β_{hL} and β_{hG} are the Lorentz and Gauss component of the total β. β_{gL}, β_{fl} are the Lorentz components of the instrument and the sample contribution, respectively and β_{gG}, β_{fG} are the corresponding Gauss components.

Profile parameters are used to calculate the Fourier coefficient (A_L) of each modeled peak corrected for the instrumental broadening. The Warren–Averbach (WA) plot, i.e. $\ln(A_L)$ vs. $(d^*)^2$ where $d^* = \frac{1}{d_{hkl}}$ is plotted to separate the size and the strain component according to WA method [36,37].

4. Results and discussion

The range of 145 MeV Ne^{6+} in SS316L was found to be around 39 μm using SRIM 2000. The total target displacements of the collision events are shown in Fig. 1. The average dpa value over a range of 39 μm for the highest dose sample was found to be $\sim 6.3 \times 10^{-2}$ and at the peak damage region, the dpa is 0.6.

4.1. Modified Williamson–Hall plot

Various parameters can be used to characterise the broadening in the conventional Williamson–Hall plots (W–H plot). ΔK is plotted as a function of the diffraction vector K for all the peaks of the unirradiated sample and also for irradiated samples at different doses of irradiation. Some typical representative figures are shown in Fig. 2. From these figures, it is seen that the points corresponding to each reflecting plane are highly scattered. Hence, it can be concluded that anisotropic broadening is present in all the samples. This anisotropy can be caused either due to the size or the strain anisotropy or as a result of both the effects. The presence of anisotropy (both size and strain) in X-ray line profile analysis means that neither the FWHM nor the integral breadths are monotonous function of the diffraction vector or its square [27–29]. So, to check the anisotropic contribution resulting from any of these effects, the modified Williamson–Hall plot is drawn which is shown in Fig. 3. Here ΔK is plotted as a function of $KC^{1/2}$. The factor $KC^{1/2}$ normalises the effect due to the anisotropic strain broadening [27–29]. The points corresponding to each reflection in modified Williamson–Hall plot (Fig. 3) should have fallen on a monotonically increasing curve according to Eq. (2) if the size broadening in the samples were isotropic. However, from Fig. 3, it is clearly seen that the point corresponding to the plane (2 0 0) does not fall on the curve for all the samples. This indicates the presence of a strong size anisotropy in the direction normal to (2 0 0) plane.

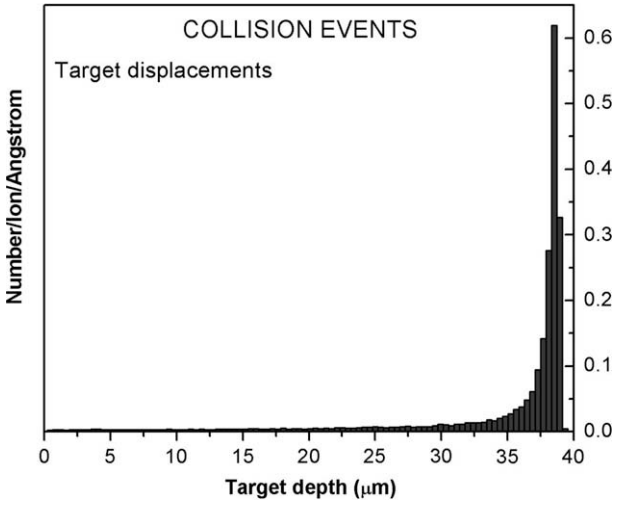

Fig. 1. Damage profile of 145 MeV Ne^{6+} in stainless steel.

In order to account for this size anisotropy, the effect of twinning and stacking fault on domain size has been considered on the basis of Eq. (3). Values of ς have been adjusted in such a way that $\Delta K - \varsigma W(K)$ follow a smooth quadratic curve according to Eq. (3). Fig. 4 shows $\Delta K - \varsigma W(K)$ vs. $KC^{1/2}$ plot for the unirradiated and three typical irradiated samples. The values of ς for the unirradiated sample and the irradiated samples at a dose of 1.0×10^{17}, 7.0×10^{18} and 2.5×10^{19} Ne^{6+}/m^2 are found to be 0.050 ± 0.006/nm, 0.042 ± 0.005/nm, 0.035 ± 0.005/nm and 0.034 ± 0.005/nm, respectively.

The density of the deformation fault (α) can be determined from the systematic shifts of the diffraction peaks relative to the annealed sample [30]. However, no systematic peak shifts have been observed for the unirradiated and the irradiated samples. This means that there are no deformation fault in the samples, i.e. $\alpha = 0$ and total faulting probability is primarily due to growth or twin faulting. This finding is in agreement with the result obtained for other material like copper with low stacking fault energy [38]. In absence of the deformation fault, the value of ς is the measure of twin faulting in the sample. Initially, the systematic decrease of ς value signifies that the twin fault probability decreases with the dose of irradiation. At higher doses of irradiation, the values of ς attained saturation. This may be attributed to the fact that the fault layers must have been affected due to the effects of irradiation by high energy heavy ions which causes highly randomized disorder within the matrix.

4.2. Pattern Decomposition using MarqX

Fig. 5 represents a typical whole powder pattern fit using MarqX for the XRD profile of Neon irradiated SS316L (20% cold-worked) sample at a dose of 7.0×10^{18} Ne^{6+}/m^2. A typical figure of WA plot at a dose of 7.0×10^{18} Ne^{6+}/m^2 is shown in Fig. 6. The $A_s(L)$ vs. L plot and microstrain ($\langle \varepsilon_L^2 \rangle^{\frac{1}{2}}$) vs. L plot (L being the Fourier length) are shown in Figs. 7 and 8 at a dose of 2.5×10^{19} Ne^{6+}/m^2 and also for the unirradiated sample. The average surface weighted domain size (D_s) is obtained from the initial slope of the $A_s(L)$ vs. L plot at all doses of irradiation. The variations of D_s and $\langle \varepsilon_L^2 \rangle^{\frac{1}{2}}$ (at L = 10 nm) as a function of dose have been shown in the insets of Figs. 7 and 8, respectively. It is seen that the size of the domain initially decreased significantly with increasing dose of irradiation and then remained almost unchanged at higher doses. Similarly, there is a decreasing trend of microstrain values with dose.

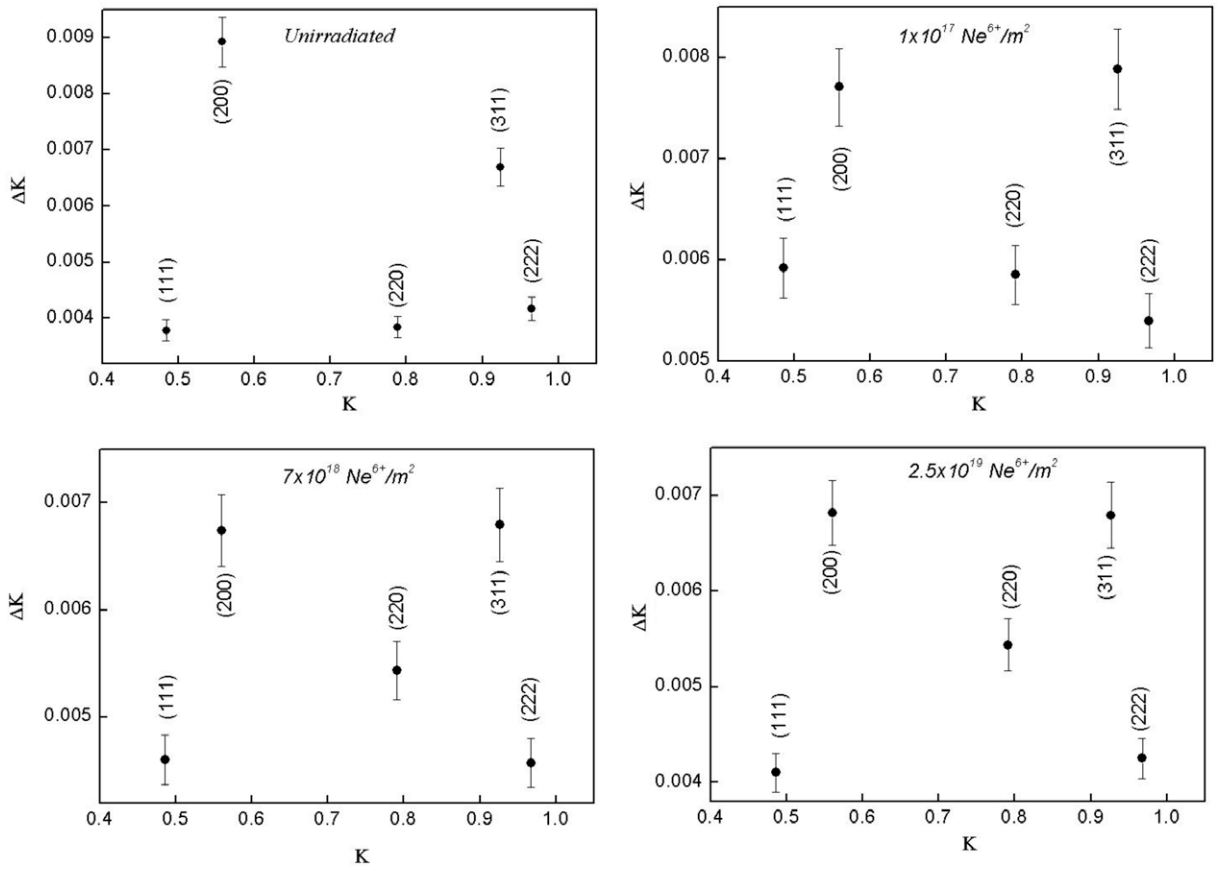

Fig. 2. Williamson–Hall plots for the unirradiated and irradiated SS316L at different doses.

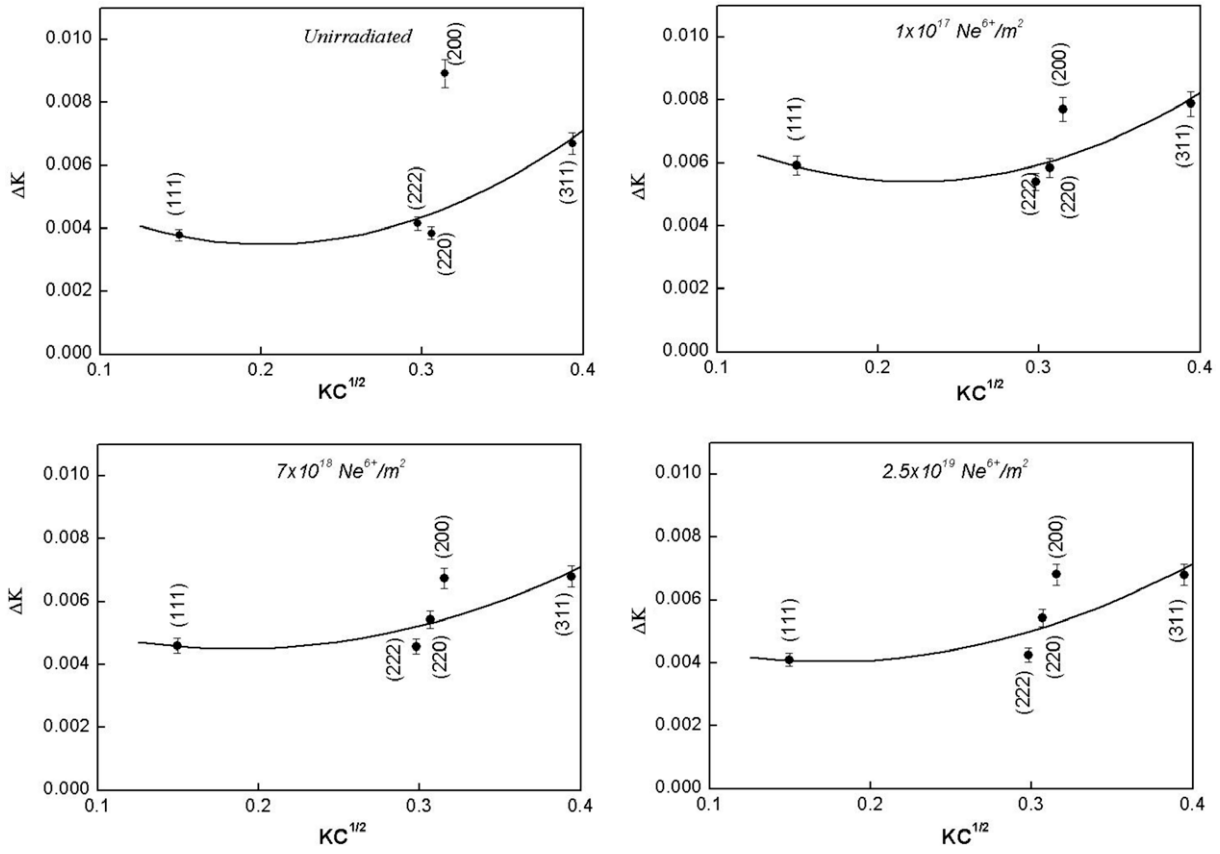

Fig. 3. Modified Williamson–Hall plots for the unirradiated and irradiated SS316L at different doses.

4.3. Modified Rietveld Technique

Figs. 9 and 10 show the variation of average D_s and $\langle \varepsilon_L^2 \rangle^{\frac{1}{2}}$ as a function of dose of irradiation. It is clearly observed that domain size reduced quite drastically up to the dose of 7.0×10^{18} Ne^{6+}/m^2 and finally attained saturation with increasing dose. The microstrain values also show a decreasing tendency with higher doses. These observations contradicted with our earlier observations during microstructural evolution in other irradiated alloys [21–23], where microstrain values always have a significant increase with increasing dose of irradiation.

Considering that the anisotropic broadening exist in both the size and the strain (as obtained by modified Williamson–Hall plot), the variations of the domain size and the microstrain along the major crystallographic directions, i.e. along ⟨111⟩, ⟨200⟩, ⟨220⟩, ⟨311⟩, as a function of dose was also obtained by this technique and are shown in Table 1. The values of the domain size and the microstrain show a decreasing trend with dose. The order of dislocation density did not change significantly with dose as shown in Table 1.

The reason of the aforementioned findings can be explained as follows.

The damage associated with the neon beam (being a heavy ion) was quite extensive and produced a highly localized concentration of defects, particularly the vacancies and the interstitials. The typical microstructural features which are expected in 20% cold-worked SS316L at low dose, are the clusters of small defects, faulted dislocation loops and pre-irradiation network of dislocation existed due to prior cold working. Due to the low stacking fault energy, the pre-irradiation dislocation network do not form cell structure but remain as dislocation arrays [39]. These individual microstructural components interact with each other as they evolve. Although a particular evolving microstructural component may approach an apparent saturation density at low fluence, but its value may be subsequently affected by the changes in another component of microstructure [13,40] like the vacancies, interstitials, etc.

The rate equations of the point defects generated during the process of irradiation are given by [41]:

$$\frac{dC_V}{dt} = K_0 - K_{iv}C_iC_v - K_{vs}C_vC_s + \nabla.(D_v\nabla C_v) \tag{7}$$

$$\frac{dC_i}{dt} = K_0 - K_{iv}C_iC_v - K_{is}C_iC_s + \nabla.(D_i\nabla C_s) \tag{8}$$

where K_0 is the radiation production, K_{iv} is vacancy–interstitial recombination rate coefficient, K_{vs} is the vacancy–sink recombination rate coefficient, K_{is} is the interstitial–sink recombination rate coefficient, C_s is the concentration of the sinks, C_v and C_i are the concentration of vacancies and interstitials respectively, D_v and D_i are the diffusion coefficient for a vacancy and an interstitial, respectively. By solving these equations without considering the diffusion term, it is found that $\tau_1 = (K_0K_{iv})^{-1/2}$ and $\tau_2 = (K_{is}C_s)^{-1}$, where τ_1 is the characteristic time up to which the linear build up of defect concentration occurs and τ_2 is the time to achieve quasi-steady state.

In the low-temperature regime, the pre-irradiation network of dislocation contributes to high sink density and as a result τ_2 becomes shorter than τ_1 [41]. This is because, at this regime, the interstitial concentration comes into a quasi-steady state with its production and annihilation within the sinks (dislocations). Hence, there is a relaxation of strain field around the network of disloca-

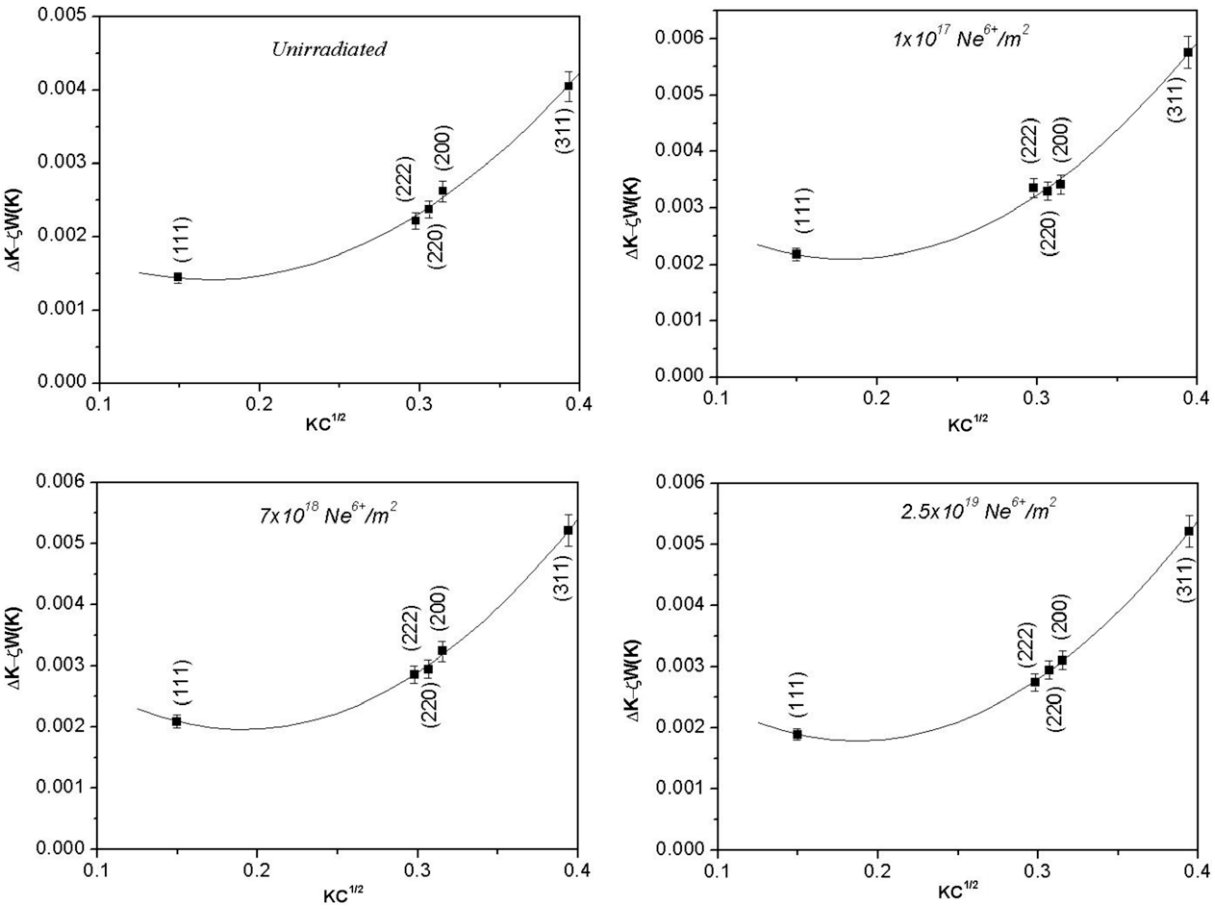

Fig. 4. Modified Williamson–Hall plots including the effect of planar faults for the unirradiated and irradiated SS316L at different doses.

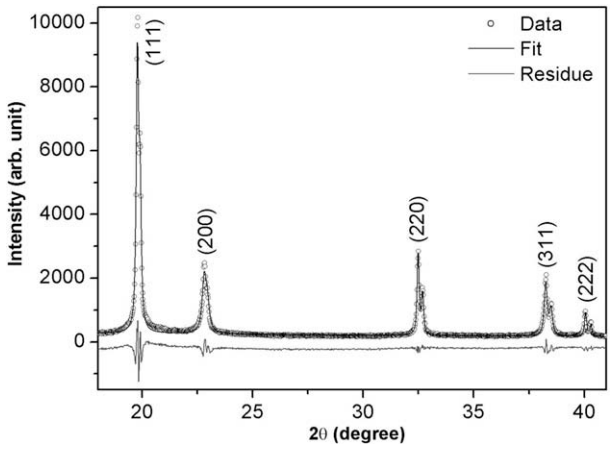

Fig. 5. A typical whole powder pattern fit using MarqX for the XRD profile of irradiated SS316L (20% cold-worked) sample at a dose of 7.0×10^{18} Ne^{6+}/m^2.

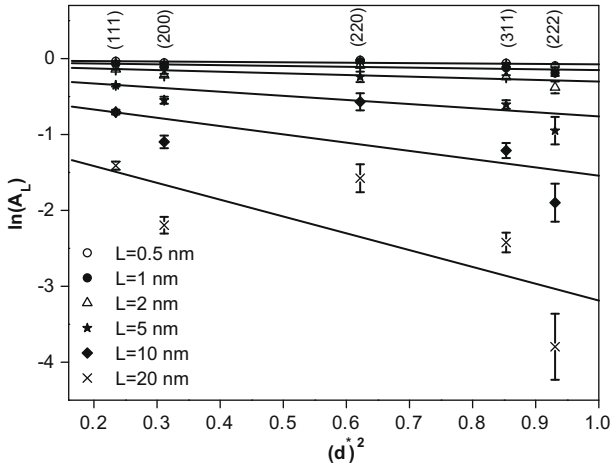

Fig. 6. A typical Warren Averbach plot at a dose of 7.0×10^{18} Ne^{6+}/m^2.

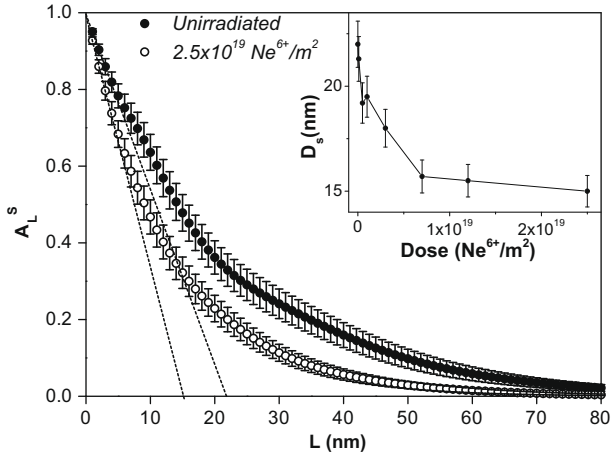

Fig. 7. $A_s(L)$ vs. L plot for the unirradiated sample and the sample irradiated at a dose of 2.5×10^{19} Ne^{6+}/m^2. The inset in the figure shows the variation of the average surface weighted domain size with dose.

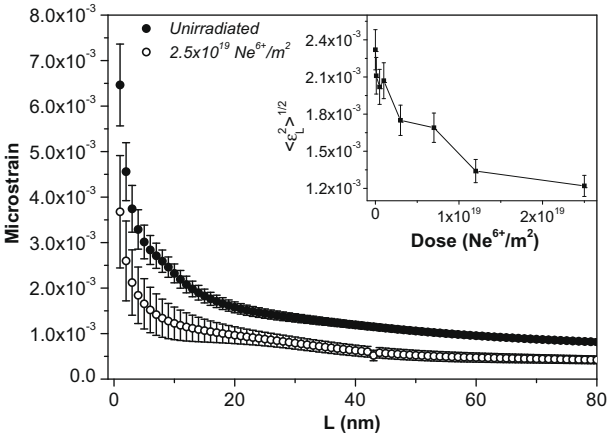

Fig. 8. Microstrain vs. L plot for the unirradiated sample and the sample irradiated at a dose of 2.5×10^{19} Ne^{6+}/m^2. The inset in the figure shows the variation of $\langle \varepsilon_L^2 \rangle^{\frac{1}{2}}$ at $L = 10$ nm with dose.

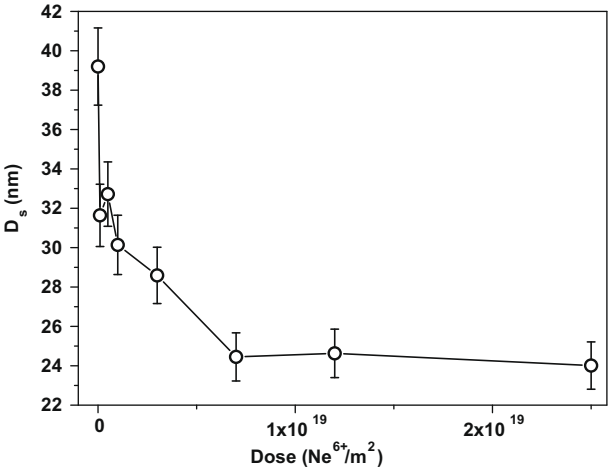

Fig. 9. Variation of average domain size as function of dose of irradiation.

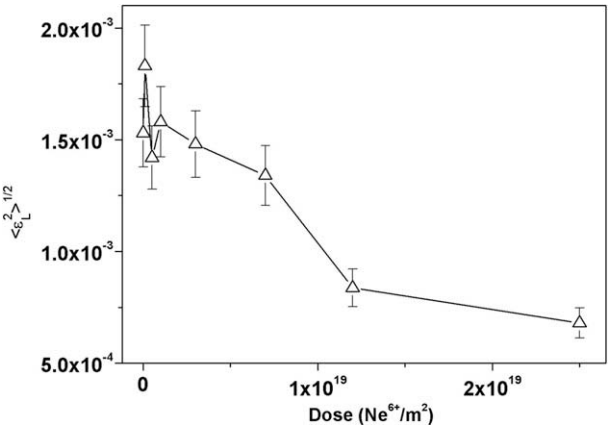

Fig. 10. Variation of average microstrain as function of dose of irradiation.

tions and the effect is manifested as a decrease in the microstrain values as observed in Figs. 8 and 10. Radiation induced recovery of the as cold-worked dislocation network at lower temperature is also observed in case of the neutron-irradiated stainless steel [42]. On the contrary, the concentration of vacancies (C_v) initially increases linearly with time during irradiation as they are relatively immobile compared to the interstitials. Moreover, irradiation with the heavy ion causes inhomogeneous damage and

Table 1
Values of domain size (D_e), microstrain (ε) and dislocation density (ρ) in the following crystallographic planes (1 1 1), (2 0 0), (2 2 0), (3 1 1) at different doses.

Dose Ne^{6+}/m^2	(1 1 1)			(2 0 0)			(2 2 0)			(3 1 1)		
	D_e (nm) ± 1.5	ε $10^{-3} \pm 5 \times 10^{-5}$	ρ $10^{15}\ m^{-2} \pm 6 \times 10^{13}$	D_e (nm) ± 1.5	ε $10^{-3} \pm 5 \times 10^{-5}$	ρ $10^{15}\ m^{-2} \pm 6 \times 10^{13}$	D_e (nm) ± 1.5	ε $10^{-3} \pm 5 \times 10^{-5}$	ρ $10^{15}\ m^{-2} \pm 6 \times 10^{13}$	D_e (nm) ± 1.5	ε $10^{-3\pm}5 \times 10^{-5}$	ρ $10^{15}\ m^{-2\pm}6 \times 10^{13}$
Unirradiated	39.1	1.3	0.9	39.7	1.0	0.7	39.3	1.3	0.9	39.5	1.1	0.8
1.0×10^{17}	32.6	1.3	1.1	35.7	1.0	0.8	34.4	1.3	1.0	34.9	1.1	0.9
5.0×10^{17}	32.8	1.3	1.1	35.4	1.0	0.7	33.5	1.2	0.9	34.7	1.1	0.9
1.0×10^{18}	32.5	1.1	0.9	33.2	1.0	0.8	34.1	0.9	0.7	33.0	1.0	0.9
3.0×10^{18}	32.8	1.1	0.9	32.6	0.8	0.7	35.6	0.9	0.7	32.7	0.9	0.8
7.0×10^{18}	26.6	1.0	1.0	33.4	0.7	0.6	30.3	1.0	0.9	31.7	0.8	0.7
1.2×10^{19}	27.5	0.8	0.7	28.1	0.8	0.8	31.4	0.6	0.5	27.9	0.8	0.8
2.5×10^{19}	23.8	0.7	0.8	26.0	0.8	0.8	27.2	0.6	0.6	25.4	0.8	0.9

produces displacement cascade consisting of highly localized interstitials and vacancies at the end of its trajectory. This creates a steep concentration gradient of defects within the range of damage (39 μm). This inhomogeneous defect concentration not only causes an enhancement of the diffusion process but also opens up new channels [41] by the creation of different defect species which are not available otherwise in thermally activated diffusion. Thus the diffusion coefficient of a particular lattice atom gets enhanced by the linear superposition of various conceivable diffusion channels [41] due to the presence of irradiation induced mono-vacancies, di-vacancies, etc. This causes an enhancement of migration of vacancies which finally cluster and collapse in the shape of dislocation loops. Zinkle et al. [13] have also reported that high density of defect clusters and dislocation loops are formed at low dose in neutron irradiated SS. These dislocation loops or defect clusters decrease the size of the domains, i.e. the coherently scattered regions as observed in Figs. 7 and 9. With increasing dose of irradiation, C_v continues to rise. A competition soon arises between the annihilation of interstitials at sinks (pre-irradiation dislocation network) and recombination with vacancies. Hence, a saturation is observed in the size of the domain at higher doses of irradiation. The formation of the dislocation loops did not change the order of the density of dislocation as the effect was compensated by the recovery of the pre-existed dislocation structure.

Using three different model-based approaches of XRDLPA techniques, the microstructure of the heavy ion-irradiated stainless steel at different doses have been characterised. For the characterisation of the microstructure of the materials, these three techniques are better used complementarily to each other rather than on their own. Conventional Williamson–Hall Technique is important in the initial stage of data analysis, when we have little knowledge about the irradiated material under investigation. Modified Williamson–Hall Technique provides information of the anisotropic size and strain in the irradiated samples. Both MarqX and Rietveld techniques are based on whole powder pattern fitting techniques including the broadening and shape of the profile while the former does not require any structural model in calculating the profile intensity. These techniques have limitations in characterising the small defects particularly small interstitial clusters which do not cause broadening of the peak but contribute to the background values close to the Bragg peak [43]. Scattering of X-rays from interstitial clusters [42,44] are diffuse scattering very close to the Bragg peak (Huang Scattering). Thus, the complete information of the microstructure of the irradiated samples can be obtained from the X-ray diffraction techniques by the combined studies of the diffraction pattern in the Bragg peak region (coherent scattering) and in the background region (diffuse scattering close to the Bragg peak). As in our case, the experiments were carried out at room temperature, the diffuse scattering near the Bragg peak region due to small interstitial clustering are superimposed by thermal diffusion scattering. Hence, the line profile analysis could characterise only those microstructural parameters which are responsible for the broadening of the diffraction peaks.

5. Conclusion

The evolution of microstructure with dose for the irradiated sample can be reliably assessed by analysing the diffraction patterns using different model-based approaches of line profile analysis, as the shape profile and the broadening of the diffraction peaks change with dose of irradiation. The domain size and microstrain were found to decrease with increasing dose of irradiation and finally attained a saturation. The high density of sinks due to the presence of pre-irradiated network of dislocation and the low mobility of point defects at room temperature must have lead to the extended transients in the concentrations of point defect and as a result, significant radiation induced recovery of the initial dislocation was observed with irradiation causing a decrease in the microstrain. Hence, it is apparent that the overall microstructural alteration is quite significant even at low doses of ion irradiation.

References

[1] C. Abromeit, J. Nucl. Mater. 216 (1994) 78–96.
[2] M.L. Bleiberg, J.W. Bemit (Eds.), in: International Conference on Radiation Effects in Breeder Reactor Structural Materials, Scottsdale, AIME, New York, 1977.
[3] H.R. Brager, J.S. Perrin (Eds.), in: International Conference on Effects of Radiation on Materials, Scottsdale, ASTM, Philadelphia, 1982.
[4] G.E. Lucas, J. Nucl. Mater. 206 (1993) 287–305.
[5] B.N. Singh, S.J. Zinkle, J. Nucl. Mater. 217 (1994) 161–171.
[6] M. Kiritani, J. Nucl. Mater. 216 (1994) 220–264.
[7] F.A. Garner, L.R. Greenwood, Rad. Eff. Deff. Sol. 144 (1998) 251–286.
[8] L.R. Greenwood, F.A. Garner, J. Nucl. Mater. 233–237 (1996) 1530–1534.
[9] F.A. Garner, B.M. Oliver, L.R. Greenwood, M.R. James, P.D. Ferguson, S.A. Maloy, W.F. Sommer, J. Nucl. Mater. 296 (2001) 66–82.
[10] B.H. Sencer, S.A. Maloy, M.L. Hamilton, F.A. Garner, J. Nucl. Mater. 345 (2005) 136–145.
[11] P.J. Maziasz, C.J. McHargue, Int. Nucl. Rev. 32 (1987) 190–219.
[12] P.J. Maziasz, J. Nucl. Mater. 205 (1993) 118–145.
[13] S.J. Zinkle, P.J. Maziasz, R.E. Stoller, J. Nucl. Mater. 206 (1993) 266–286.
[14] T.R. Allen, J.I. Cole, C.L. Trybus, D.L. Porter, H. Tsai, F. Garner, E.A. Kenik, T. Yoshitake, Joji Ohta, J. Nucl. Mater. 348 (2006) 148–164.
[15] Y. Isobe, M. Sagisaka, F.A. Garner, S. Fujita, T. Okita, J. Nucl. Mater. 386–388 (2009) 661–665.
[16] P. Mukherjee, A. Sarkar, P. Barat, S.K. Bandyopadhyay, Pintu Sen, S.K. Chattopadhyay, P. Chatterjee, S.K. Chatterjee, M.K. Mitra, Acta Mater. 52 (2004) 5687–5696.
[17] T. Ungar, H. Mughrabi, D. Rönnpagel, M. Wilkens, Acta Metall. 32 (1984) 333–342.
[18] T. Ungár, J. Gubicza, P. Hanák, I. Alexandrov, Mater. Sci. Eng. A 19–321 (2001) 274–278.
[19] J. Gubicza, L. Balogh, R.J. Hellmig, Y. Estrin, T. Ungár, Mater. Sci. Eng. A 400–401 (2005) 334–338.
[20] P. Mukherjee, P.M.G. Nambissan, P. Barat, Pintu Sen, S.K. Bandyopadhyay, J.K. Chakravartty, S.L. Wadekar, S. Banerjee, S.K. Chattopadhyay, S.K. Chatterjee, J. Nucl. Mater. 297 (2001) 341–344.
[21] P. Mukherjee, P. Barat, S.K. Bandyopadhyay, P. Sen, S.K. Chottopadhyay, S.K. Chatterjee, M.K. Mitra, J. Nucl. Mater. 305 (2002) 169–174.
[22] P. Mukherjee, A. Sarkar, P. Barat, Mater. Char. 55 (2005) 412–417.
[23] P. Mukherjee, A. Sarkar, P. Barat, Baldev Raj, U. Kamachi Mudali, Metal Mater. Trans. A 36A (2005) 2351–2360.
[24] J.P. Biersack, L.G. Haggmark, Nucl. Instrum. and Meth. Res. B 174 (1980) 257–269 (The Stopping and Range of Ions in Matter (SRIM 2000) software developed by J. Ziegler, J.P. Biersack is available on the website: <http://www.research.ibm.com/ionbeams>).
[25] J.I. Langford, D. Lauer, Rep. Prog. Phys. 59 (1996) 131–234.
[26] G.K. Williamson, W.H. Hall, Acta Metall. 1 (1953) 22–31.
[27] T. Ungár, A. Borbély, Appl. Phys. Lett. 69 (1996) 3173–3175.
[28] A. Révész, T. Ungár, A. Borbély, J. Lendvai, Nanostruct. Mater. 7 (1996) 779–788.
[29] T. Ungár, S. Ott, P.G. Sanders, A. Borbély, J.R. Weertman, Acta Mater. 46 (1998) 3693–3699.
[30] B.E. Warren, Prog. Metal Phys. 8 (1959) 147–202.
[31] L. Lutterotti, P. Scardi, J. Appl. Cryst. 23 (1990) 246–252.
[32] G.K. Williamson, R.E. Smallman, Philos. Mag. 1 (1956) 34–46.
[33] Y.H. Dong, P. Scardi, J. Appl. Cryst. 33 (2000) 184–189.
[34] J.I. Langford, in: E. Prince, J.K. Stalick (Eds.), Accuracy in Powder Diffraction II. NSIT Special Publication 846, USG Printing Office, Washington, 1992, pp. 110–126.
[35] M. Ahtee, L. Unonius, M. Nurmela, P. Suortti, J. Appl. Cryst. 17 (1984) 352–357.
[36] B.E. Warren, X-ray Diffraction, Addison-Wesley, Reading, MA, 1969.
[37] B.E. Warren, B.L. Averbach, J. Appl. Phys. 21 (1950) 595–599.
[38] P.G. Sanders, A.B. Whitney, J.R. Wreetman, R.Z. Valiev, R.W. Siegel, Mater. Sci. Eng. A 204 (1995) 7–11.
[39] D.A. Hughes, D.C. Chrzan, Q. Liu, N. Hansen, Phys. Rev. Lett. 81 (1998) 4664–4667.
[40] R.E. Stoller, G.R. Odette, in: F.A. Garner, N.H. Packan, A.S. Kumar (Eds.), ASTM STP 955, ASTM, Philadelphia, 1987, p. 371 (Part I).
[41] R. Sizmann, J. Nucl. Mater. 69–70 (1978) 386–412.
[42] P.J. Maziasz, J. Nucl. Mater. 191–194 (1992) 701–705.
[43] J.B. Roberto, B. Schoenfeld, P. Ehrhart, Phys. Rev. B 18 (1978) 2591–2597.
[44] P. Ehrhart, J. Nucl. Mater. 69–70 (1978) 200–214.